The Search for Coherent Structures in Turbulence

A Thesis Proposal
Presented to
The Academic Faculty

by

Christopher J Crowley

In partial fulfillment
of the requirements for the
Doctor of Philosophy in Physics

Georgia Institute of Technology
August 2020

CONTENTS

I. INTRODUCTION

Nearly every flow in the universe is turbulent. Turbulence dominates flows on a vast range of length scales in both naturally occurring and man-made settings. From the spectacular flow within a nebula to the atmospheric jet-streams in weather to the air rushing past a car on the highway to the blood pumping through the aorta with every heartbeat, the flows we interact with and are interested in understanding are all turbulent. Turbulence is the prime source of difficulty in nearly all engineering or scientific endeavors involving fluid flows such as weather prediction, aerodynamic design, and industrial chemical mixing.

Despite the extreme prevalence of turbulence in flows around us, turbulence has remained one of the longest unsolved problems in classical physics. Understanding the complicated motion of an unsteady flow has eluded scientists since the first scientific theory of turbulence was proposed by Leonardo da Vinci more than 500 years ago [1]. Nearly 300 years after da Vinci, the Navier-Stokes (NS) equations were derived, which describe the time rate of change of a fluid's velocity everywhere in the flow [2]. Physicists and mathematicians have been trying to determine ways to solve the NS equations in parameter regimes where turbulence is present. The challenge with the NS equations is that they are nonlinear partial differential equations and the mathematical machinery necessary for dealing with these types of problems is, for the most part, nonexistent.

Most existing approaches to understanding turbulence are statistical ones. These approaches treat turbulence as a random fluctuation on top of the mean flow. The fluctuations can be modeled a number of ways, but ultimately the stochastic nature of the fluctuations makes understanding the time evolution of turbulence difficult.

Despite the stochastic nature of classical turbulence modeling, experiments have revealed that ordered structures do, in fact, exist within turbulence suggesting it is possible to develop a model based on specific flow patterns. The structures being observed occur often enough that fluid dynamicists are able to reliably identify and name them [3, 4]. These characteristic flow patterns, called Coherent Structures, are regions of the flow that have features that persist for a significant duration of time. Many Coherent Structures have been identified, but two of the most commonly studied are quasi-streamwise rolls [5] and hairpin shaped vorticies [6]. There are theories about the role Coherent Structures play in turbulence [7, 8], however they are all phenomenological and are not easily connected to the governing equations.

Recently, a new approach to understanding Coherent Structures in turbulence based on first principals and tied directly to the NS equations has been developed. This new approach relies on numerically computing special nonchaotic solutions to the NS equations and analysing their dynamics. This approach has emerged from the field of dynamical systems theory and makes use of the observation that, embedded within the complicated dynamics of chaotic systems there exist simpler, nonchaotic solutions to the governing equations that guide the chaotic dynamics [9–16]. These nonchaotic solutions are thought to be the precise solutions to the NS equations that coherent structures observed in turbulence are mimicking [10]. These special solutions are often called Exact Coherent Structures (ECSs). With a sufficient number of ECSs in hand, the time evolution of the turbulence may be able to be approximated.

To investigate the use of ECS theory in an experimentally observed turbulent flow, we will be looking at a weakly turbulent flow in a Taylor-Couette geometry. Taylor-Couette flow (TCF) is the flow between two coaxial, independently rotating cylinders (see Fig. 1). The TCF is ideally suited to study the dynamical systems approach to turbulence because it is able to be investigated in the numerics without approximation or ambiguity (i.e. direct numerical evaluation of the NS equations with the actual physics at the boundary of the TCF cell). Additionally, experimental measurements of the turbulent velocity field can be made over a large portion of the flow domain.

In this proposal I will discuss some relevant background information as well as preliminary work before presenting the work I propose completing for my thesis. I will first give a brief introduction to the theoretical framework and tools that will be used in the proposed research in section II. Then, in section III I will discuss the important case in which the height aspect ratio in TCF becomes small and the axial end effects play a role in the dynamics of the turbulent transition (specifically in a system with a ratio of height to gap width of 5.26). Finally, in section IV I will propose new research in TCF with a ratio of height to gap width of 1 that, together with the work in a ratio of height to gap width of 5.26, will make up the content of my thesis.

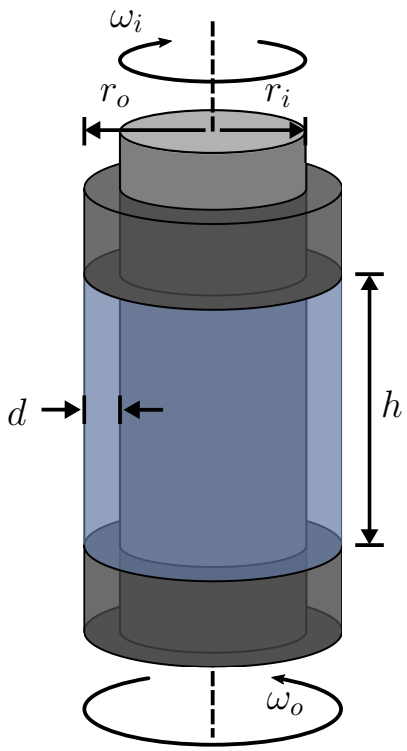

FIG. 1. In Taylor-Couette flow, a fluid is confined between coaxial cylinders of radii r_i and r_o, which counter-rotate with angular velocities ω_i and ω_o, respectively. In the axial direction, the flow is bounded by two end caps that rotate with the outer cylinder and are separated by a distance h. In the radial direction, the separation between the cylinders is $d = r_o - r_i$. The flow is periodic in the azimuthal direction. Figure taken from Crowley *et al.* [17]

II. BACKGROUND

A. Dynamical systems

There are two different mathematical approaches commonly used when solving for the dynamics of a physical system. One method involves deriving a differential equation relating coordinates to their derivatives and the other is to derive a set of coupled differential equations describing the time rate of change (i.e. first time derivative of) each coordinate. If, for instance, the system in question is a mechanical system, then the traditional approach, stemming from Newton's second law, is to describe the system in terms of coordinates and solving a differential equation relating these coordinates to their second derivatives in time. For example, a simple pendulum can be described by measuring the angle made between the bob and the direction of gravity, θ, and the acceleration of this angle, $\ddot{\theta}$. With this coordinate and its acceleration, a differential equation relating the two can be written down:

$$\ddot{\theta} = -\frac{g}{l}\sin[\theta] \tag{1}$$

where g is the local gravitational acceleration and l is the length of the pendulum. There are powerful methods for deriving these differential equations (e.g. variational techniques), but often analysing the resulting equation for complicated systems is difficult. There is another approach, pioneered by Henri Poincaré in the late 19th century, that utilizes the same coordinates. Instead of deriving equations relating coordinates to their accelerations, this alternate approach derives a system of differential equations describing the time rate of change of each of these coordinates and their velocities [18, 19]. This coupled set of differential equations

is called a dynamical system. For the simple pendulum case this system these equations would be:

$$\begin{aligned} \dot{\theta} &= v_\theta \\ \dot{\omega}_\theta &= -\frac{g}{l}\sin[\theta]. \end{aligned} \tag{2}$$

This second procedure, though mathematically equivalent to the first, is intuitively different and lends itself easily to more powerful analysis techniques.

Expressing the physics in this dynamical systems way suggests that a natural way of understanding the dynamics is to consider a point moving around in the space of coordinates and their associated velocities. Since the governing equations are expressed as total time derivatives of the coordinates and their velocities, each coordinate and velocity can be thought of as its own independent variable. By constructing a space where each dimension is a different coordinate or coordinate velocity, the complete state of the system at an instant in time can be represented as a single point. This space is often called state space and the governing equations describe how this point moves in time throughout it. As time evolves, the point traces out a curve and the shape of this curve is influenced by the special geometric objects within state space.

To illustrate how the system behavior in state space is guided by geometrical objects, consider an example of a purely mathematical system: the 2D Lotka-Volterra system [20]. In the Lotka-Volterra, the "coordinates" are the total population of species 1, x_1, and species 2, x_2. The specifics of the dynamical system depend on details of the two species and their interaction. One such system may look like:

$$\begin{aligned} \dot{x_1} &= x_1\left(3 - x_1 - 2x_2\right) \\ \dot{x_2} &= x_2\left(2 - x_1 - x_2\right). \end{aligned} \tag{3}$$

In this system, the linear term is exponential growth (i.e. 2 becomes 4 which becomes 8 and so on), the $-x_i^2$ term captures intra-species competition, which prevents the population from growing indefinitely, and the cross-term $-x_1x_2$ captures inter-species competition. By knowing x_1 and x_2 at an instant in time, in principle, the time evolution of the system can be determined for all time. However, as the nonlinearity grows, the evolution of x_1 and x_2 can be very complicated and slight changes in the initial known values can result in wildly different time evolution. To see why this may be the case, consider a plot shown in Figure 2 where each point in the x_1-x_2 plane represents a different state of the system. The arrows and their spacing on this plot represent which direction and how fast the system will move in the next time instant. Now, consider the situation in which the starting configuration of the system is very close to (but not exactly) at $(x_1, x_2) = (1, 1)$. In the vicinity of this location, the dynamics can be linearized and the directions along which the dynamics push or pull trajectories towards this point (i.e. eigendirections) can be determined. If the initial condition was not on the point $(1, 1)$ or along either of its eigendirections, then depending on which eigenvector it was closest to, the time evolution would race off to different regions of state space.

In state space, there are key solutions to the governing equations which are simple in time that play an important role in describing the systems' behavior within state space. The point (1,1) is an example of one such solution such that if the system is found with that configuration, then it will remain in that configuration as time evolves. These special points are called fixed points and their time evolution is invariant to the dynamics of the system (i.e. they remain unchanged by the dynamical systems governing equation). These invariant solutions to the governing equations help shape the structure of state space. Linearized dynamics in the neighborhood of these invariant solutions generically fall into three types: stable (an attracting solution), unstable (a repelling solution), and a saddle (hyperbolic solution). In Figure 2, the fixed-point A is an unstable equilibrium solution that repels all trajectories in its vicinity. Similarly, the fixed-point solutions B and D are stable equilibria that attract nearby trajectories along all directions. The dynamics in the neighborhood of these two types of solutions are relatively simple and as far as dynamics are concerned, boring. The fixed-point solution C, however, attracts trajectories along some directions and repels them along others; this type of solution is a hyperbolic equilibrium (or a saddle). Invariant solutions, in general, are solutions whose dynamics are simple (or recurrent) in time. Another common example of an invariant solution is a periodic orbit in which the state returns to itself after a fixed, finite amount of time T (i.e. $x_i(t) = x_i(t+T)$). In general, invariant solutions come in many different topologies, but the present research is only focusing on the simplest of these topologies.

Beyond the solutions themselves, stable/unstable manifolds form dynamical connections linking regions of state space. That is, an initial condition placed along certain unstable directions of an invariant solution will

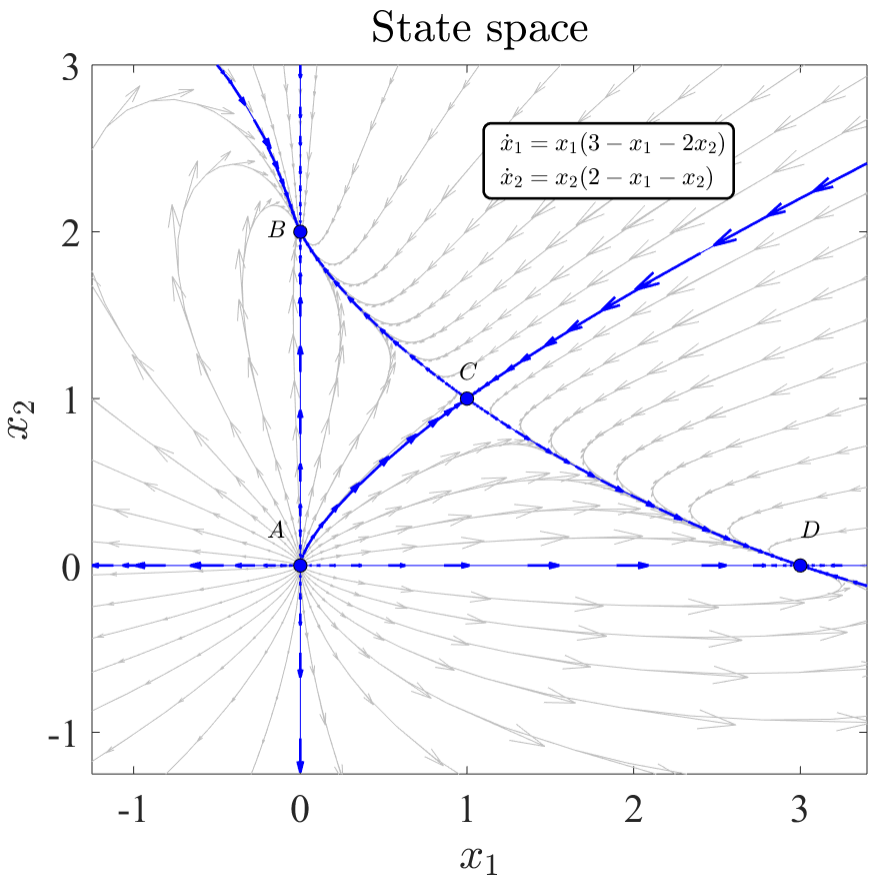

FIG. 2. Example 2D state space of a nonchaotic flow map. The dynamics shown here are from the Lotka-Volterra (competition model) relations. The fixed-point A is a repeller, while fixed-points B and D are attractors and C is a unstable hyperbolic fixed-point (or, saddle). The blue lines with arrows indicating flow direction, are dynamical connections between the solutions.

move away from the solution beyond the linear neighborhood and eventually land on the stable direction of another solution. One class of these special curves, known as heteroclinic orbits are shown in blue in Figure 2. This means that a trajectory that visits the neighborhood of one hyperbolic unstable solution could get kicked away from it and travel along its unstable direction and continue along its nonlinear extension. If the state space geometry along the heteroclinic orbit is not too unstable itself, the trajectory could travel along the orbit until it reaches the neighborhood of the invariant solution on the other end of the connection. In this way, the invariant solutions not only shape the local geometry of state space, but their connections form a network that ties together different regions of state space. As the dimensionality of state space grows, these lower dimensional entities (i.e. invariant solutions and their connections) remain the objects that guiding the dynamics in state space.

State space describing a fluid flow is very large (i.e. high dimensional). For a fluid, every fluid element in the flow has its own velocity. This means that describing its dynamics requires a coordinate and velocity for every point in the flow. The resulting state space is very high dimensional. In principal, a fluid is a continuum of fluid elements and thus would need an infinite number of coordinates and velocities and therefore an ∞-dimensional state space. In practice, however, viscosity causes structures with short length scales to dissipate very quickly. This means that there is a smallest length scale, set by the viscosity, that is relevant in the fluid flow so state space does not need to be ∞-dimensional, but rather, just a very large number of dimensions [21].

The invariant solutions in the high dimensional state space describing a fluid corresponds to flow patterns

in the 3D physical space the fluid lives in. These special flow patterns are the ECS discussed in Section I. They are unstable flows and therefore will not be exactly present in a turbulent flow, but the turbulent flow may come near to them in state space temporarily. This means that a turbulent flow will fleetingly resemble the ECS. A primary objective of the proposed work in this thesis is to test this conjecture about the role of ECS in laboratory turbulence that takes place in three spatial dimensions—specifically, in the turbulent flow between rotating cylinders–turbulent Taylor-Couette flow.

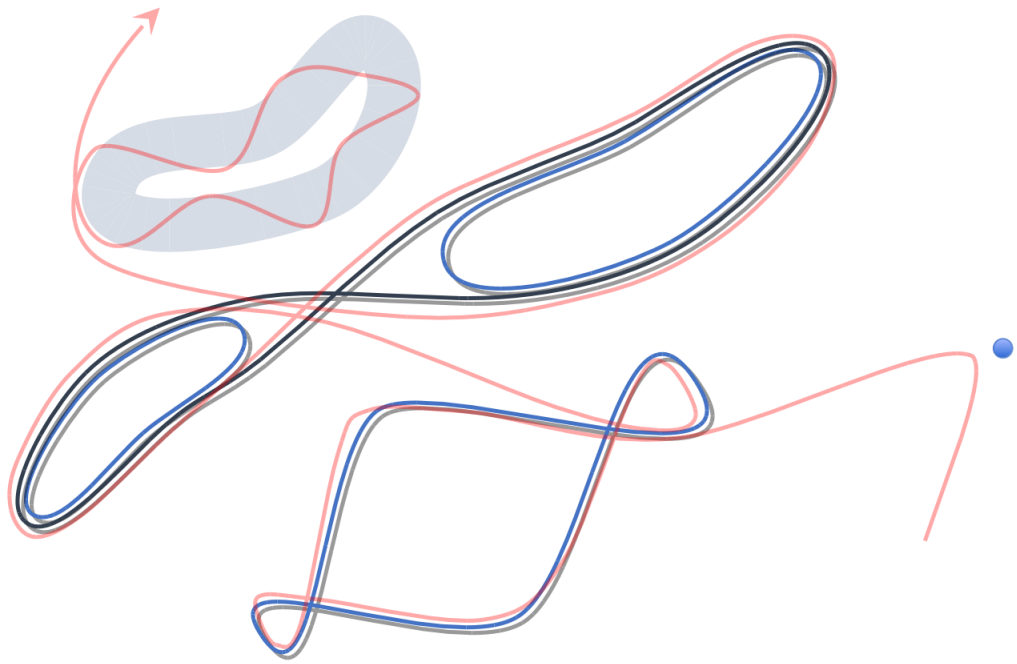

FIG. 3. A schematic representation of the hierarchy of state space structures. The red curve represents a turbulent trajectory and the blue structures represent ECS.

B. Taylor-Couette flow

Taylor-Couette flow, or the flow between two coaxial, independently rotating cylinders (see Figure 1), is fully characterised by its geometric and fluid properties. Taylor-Couette flow (TCF) can be uniquely characterized by four nondimensional parameters. Two parameters characterize the geometry of the system: the radius ratio $\eta = r_i/r_o$, where r_i and r_o are the radii of the inner and outer cylinders, respectively, and the aspect ratio $\Gamma = h/d$, where $d = r_o - r_i$ is the radial separation distance between the cylinders and h is the axial height of the flow domain. The other two parameters, the inner and outer Reynolds numbers $Re_{i,o}$, describe the cylinders' rotation rates and are given by

$$Re_{i,o} = \frac{r_{i,o}\,\omega_{i,o}\,d}{\nu}, \tag{4}$$

where ν is the kinematic viscosity of the fluid and $\omega_{i,o}$ are the angular velocities of the inner and outer cylinders, respectively. By convention Re_i is always taken to be positive, whereas Re_o is positive when the cylinders are co-rotating and negative when they are counter-rotating.

Centrifugal effects can cause the flow to become unstable. If the inner cylinder rotates, there will be a centrifugal force acting on the fluid. If the radial pressure gradient is greater than or equal to this force, a fluid element displaced in the radial direction experiences a restoring force and the fluid flow is stabilized. If, however, the pressure gradient cannot balance the centrifugal force, a fluid element displaced in the radial

direction will not experience a restoring force, but instead, continue to be forced away from its original position. This criterion for stability is known as the Rayleigh criterion [22, 23] and if the fluid does not meet this criterion it is considered to be centrifugally unstable. In TCF this criterion works out to be $Re_i \geq \frac{1}{\eta} Re_o$ for the base flow. This criterion, however, implies that for a stationary outer cylinder and just a very slow inner cylinder rotation, the base flow would be unstable. The Rayleigh criterion neglects viscosity which was found by Taylor to have a stabilizing effect [24]. Using linear stability analysis Taylor calculated when the base flow becomes unsteady as a function of Re_o and Re_i. This calculation also showed that the base flow was stable for all values of Re_o and a stationary inner cylinder.

When the cylinders' rotation rates increase beyond the initial stability threshold, additional instabilities cause the formation of numerous different, non-turbulent flow states. These flow states were first predicted and experimentally studied by G. I. Taylor in 1923 [24]. Taylor investigated these flow states by photographing the stream lines traced out by fluorescent dye injected into the flow. In Taylor's own words, this technique is considerably difficult. In 1956, to further understand what was going on within the flow, Schultz-Grunow and Hein seeded the flow with aluminum flakes they extracted from hammer paint [25]. Due to their anisotropic shape, the aluminum flakes preferentially align with the gradient in the flow resulting in regions of the flow that reflect more or less light depending on the local gradient in the flow. This technique allowed Schultz-Grunow and Hein to visualize transitions in the flow beyond the initial stability threshold. This same technique was later used by Andereck *et al.* [26] to discover a myriad of stable, non-turbulent flow states (see Figure 4 for examples) for different rotation rates (see Figure 5). This flow visualisation technique has come to be known as rheoscopic flow visualization with modern experiments being carried out very similarly with the use of more neutrally buoyant particles [27].

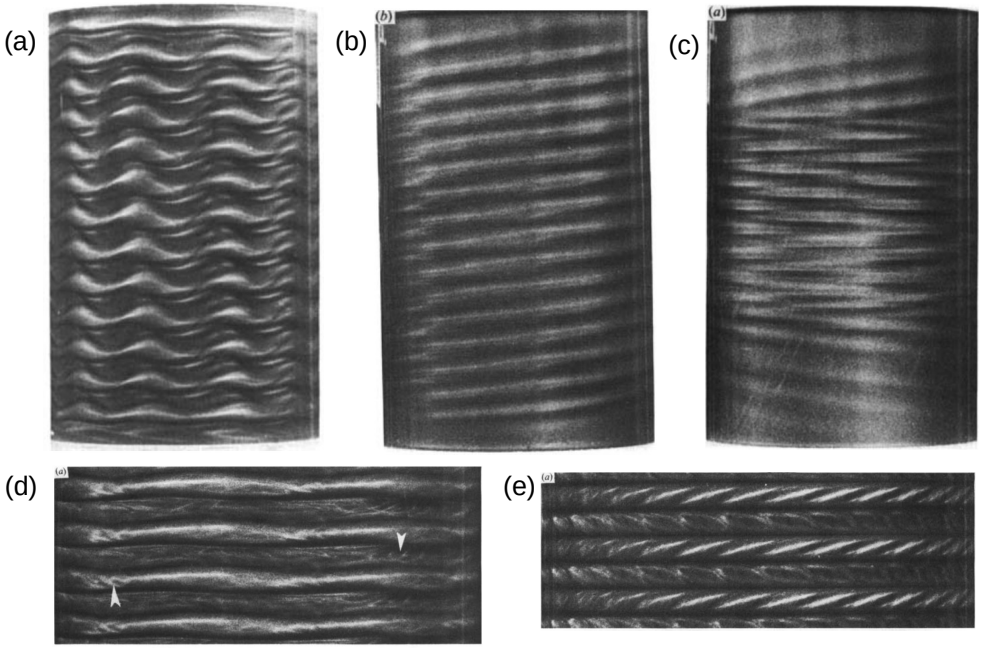

FIG. 4. Example flow visualization of non-turbulent stable flow states observed in TCF. (a) Modulated wavy vortex flow. (b) Laminar spiral flow. (c) Interpenetrating spiral flow. (d) Rippled wavy-Taylor-vortex flow with arrows pointing to the ripples. (e) Twisted Taylor vertices. To see what values of Re these flow states occur, refer to Figure 5. These images are taken from Ref. [26].

When the rotation rates are sufficiently fast, the flow transitions into turbulence through one of two ways. TCF has mostly only been studied in the large Γ limit with inner cylinder rotation dominating. The transition to turbulence in the large Γ limit is not directly from laminar, but instead the flow passes through a series of stable flow states. This is unlike the turbulent transition observed in shear driven flows such as in pipes or over an airplane wing which is directly from laminar. Because of this, TCF turbulence is not often studied in the transitional region; it is typically studied in the high Re regime where the transition dynamics

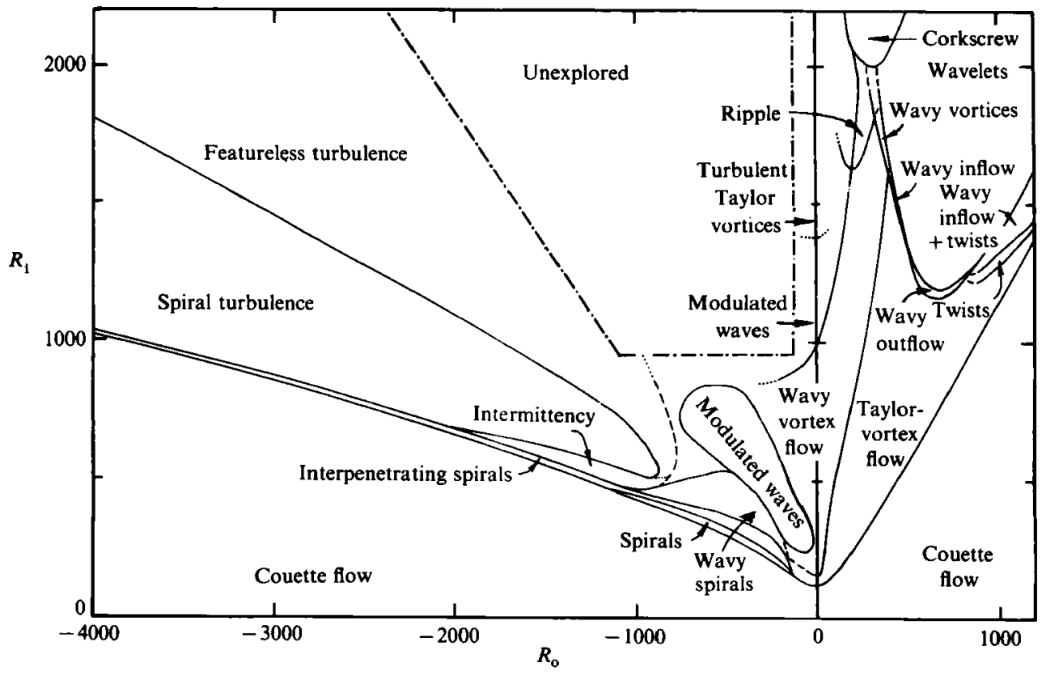

FIG. 5. Flow state transition map for a TCF with a large Γ and $\eta = 0.883$. The horizontal axis corresponds to Re_o and the vertical corresponds to Re_i This diagram was generated by first setting the Re_o, then quasi-statically increasing Re_i and recording when the transition occurred. This figure comes from Andereck *et al.* [26].

are not important. There are, however, scenarios in TCF that exhibit direct laminar to turbulent transitions akin to those observed in wall-bounded shear flows. If, for example, the outer cylinder rotation dominates, linear stability analysis of the symmetric flow suggests that no transition will occur. At sufficiently high Re_o a spontaneous transition to turbulence is observed [28–30]. This transition is not due to the change in stability of a base flow, but rather due to the nonlinear growth of finite amplitude disturbances. These studies have all been in systems with a large Γ where end effects from the top and bottom end caps can mostly be ignored.

The small Γ regime is important in the work investigated here, however, little is known about how TC becomes turbulent in small Γ systems. In order to make comparisons between fully resolved numerical simulations with the same boundary conditions as in the experiment, the flow domain must be small to enable tractable calculations. In the discussion above, the description of turbulence has focused on the regime where the aspect ratio is large. There have been few studies focused on turbulence when Γ is small. As Γ decreases, the end effects begin playing a more substantial role in the dynamics and the overall picture changes. The presence of the top and bottom end caps result in a global secondary flow in the r-z plane analogous to geophysical Ekman circulation. This secondary flow acts to redistribute angular momentum and as Γ becomes small, this happens so much that the base flow no longer resembles the base flow in the large Γ system. The transition away from the laminar base flow occurs at a larger value of Re_i as Γ decreases [31]. An exploration of how this transition changes for a system with a small Γ is presented in section III.

Much of the understanding of TCF discussed so far has relied heavily on the intuition afforded to researchers by flow visualization. In order to test the dynamical systems description of turbulence described in section II A, a more quantitative observation technique is needed.

C. Velocimetry

The discussion of fluid dynamics experiments so far has relied on qualitative observations of the flow, mostly using rheoscopic flow visualization techniques. However, a technique is needed to capture quantitatively, the time-resolved, instantaneous state of a turbulent flow that is present in the dynamical systems picture of turbulence. There are numerous quantitative measurement techniques that offer velocity information about the flow.

Quantitative flow velocimetry techniques can be split up into two categories: techniques where the velocity is either inferred from measurements of intrinsic fluid properties or measurements of movement of tracer particles dispersed in the fluid. Techniques based on intrinsic fluid properties measure, for instance, the fluid's instantaneous pressure (e.g. pitot tubes), the ability for the fluid to absorb heat (e.g. hot-wire), the speed of sound (e.g. acoustic techniques), or the index of refraction (e.g. schlieren). These techniques typically obtain time dependant velocity information that is localized in space which requires approximations to extrapolate to obtain a spatially extended flow state. Similarly, many of the techniques that use tracer particles, obtain spatially localized velocity information (e.g. LDV and acoustic particle Doppler) as well. However, there are tracer based techniques which rely on imaging the instantaneous distribution of particle locations via a camera. There are numerous image velocimetry techniques such as Optical Flow, Motion Enhancement, Particle tracking, and Particle Image Velocimetry (PIV). Because image velocimetry techniques offer instantaneous, spatially extended velocity information, they are ideal candidates for experiments exploring the dynamical systems description of turbulence. The work discussed in this proposal will utilize several variants of PIV.

PIV is a measurement technique where successive images of flows that have been seeded with tracer particles are analyzed in order to obtain particle displacements. The displacement of the tracer particles are assumed to track well with the fluid volume surrounding the particle. There are many considerations that need to be thought of before implementing this technique and are discussed in many texts [32, 33]. A successive pair of images obtained from a camera capture light intensity distributions from the flow impinging on the cameras' sensors at two neighboring instants in time. PIV does not capture the specific locations of individual particles, but instead, works entirely with the light intensity field obtained on the camera image.

Regardless of the implementation, all PIV algorithms operate on the same principal. The PIV algorithm splits the light intensity distribution from the flow at one instant in time up into sub-regions and performs a cross-correlation of that sub-region with the full light intensity distribution obtained in the next instant in time in order to determine the light intensity patterns' local spatial shift. The standard implementation of PIV relies on the particle pattern – and therefore the light pattern – remaining largely undeformed between two frames with only a lateral shift between them.

Since particles seeded in a 3D flow will be distributed throughout the whole 3D volume, the location of the particles in the dimension perpendicular to the image needs to be known in order to obtain accurate particle displacement. Without this additional spatial information, there is no way to obtain a coherent light intensity pattern displacement. Obtaining the additional spacial information can be achieved in several different ways. In the following subsections two of these methods will be discussed; one method to obtain the two components of velocity within a 2D sheet (2D-2C) and a method to obtain the full three components of velocity in the full flow volume.

D. 2D planar PIV (2D-2C)

In 2D PIV, the particles being used to probe the velocity field are confined to a single plane (or, thin curved surface in some cases[34]) typically by confining the illuminating light to a thin sheet. With only a single plane of particles being illuminated, the camera can be setup perpendicular to this illumination sheet, removing the ambiguity of the particles position in the third dimension. Two successive images obtained in this way can be directly split into sub-regions and cross-correlations performed in the standard PIV implementation. Like with any PIV algorithm, the quality of the input images is crucial. High quality images can be obtained by image preprocessing where filters are implemented to enhance signal-to-noise ratios of the particles. The highest quality PIV occurs when the raw images themselves have high a signal-to-noise ratio which can be achieved with careful setup of the illuminating optics. For best results with PIV, the images will have uniform lighting, clear separation between particle and background intensities,

and particle intensities that remain constant in time (e.g. they are not anisotropic and tumbling or moving perpendicular through the light sheet).

By establishing the plane by simply cropping the illuminating light into a sheet, particles are only illuminated when they are in the light sheet and therefore will only contribute to the correlations when they are in the plane. As long as the velocity is mostly in line with the plane, then particles will remain in the illumination long enough for a correlation to be determined. If, however, there is a substantial component of the velocity perpendicular to the plane, particles will appear and disappear on the image in a seemingly random way making a correlation impossible. This can be mitigated by either increasing the thickness of the light sheet, aligning the illumination plane with the maximum velocity, or by increasing the frame rate of the camera.

E. 3D tomographic PIV (3D-3C)

Tomographic Particle Image Velocimetry, or tomo PIV, is a velocimetry technique where a 3D volume of light intensity is first reconstructed, then 3D cross-correlations are carried out to find the most likely displacement. In tomo PIV, multiple cameras simultaneously image a particle seeded flow from various angles. A 3D light intensity distribution is then calculated from these images using an iterative reconstruction algorithm [35, 36]. A 3D cross-correlation is then performed against two successive in time subregions of the reconstructed intensity field and a 3D grid of 3-component velocity vectors are produced [37]. If the density of particles on each individual image is too high, the reconstruction algorithm will produce erroneous peaks in the reconstructed field called ghost particles. Since these ghost particles have nothing to do with the flow and are just artifacts of the reconstruction, they diminish the quality of the measurement. As the seeding density is increased the number of ghost particles also increases [38] and in practice the highest seeding density that is possible for tomo PIV is about 0.5 particles per pixel [36].

Though tomo PIV is a high fidelity technique, it is a few serious draw backs. Tomo PIV is a high quality technique for computing 3D velocity fields; however, it requires not only reconstructing a 3D intensity array at each timestep, but it also requires performing many cross-correlations in the 3D space. These calculations are demanding, requiring a lot of computational power to determine a single snapshot in time, let alone an entire time series. Similarly, each snapshot in time produces a 3D array of velocity measurements which takes up a lot of disk space and is cumbersome to analyze. If adequate computational power is available, there are still drawbacks such as the increased noise from ghost particles [37] and by representing the light intensity field on a 3D gridded voxel space, there are discretization errors on the particles locations [36] Additionally, cross-correlation applies spatial averages over the subregion volumes and therefore smooths out velocity gradients and fine flow structures. This effect can be slightly mitigated with the use of Gaussian [39] or adaptive [40] weighting in the correlation process, but cannot be fully removed.

III. TRANSITION TO TURBULENCE IN SMALL ASPECT RATIO TCF

The transition to turbulence in TCF is typically thought of as occurring through a series of bifurcations of simpler, non-turbulent states. However, as Γ gets smaller, the end effects begin playing a key role and the transition begins resembling the transitions to turbulence observed in shear driven flows (e.g. pipes, channels, and boundary layers). To explore this, lets first look at at a TCF system where the end effects are important but do not dominate the flow. In $\Gamma = 5.26$ TCF exhibits a novel transition to turbulence that is mediated by an intermediate, stable flow state. In the following sections we will discuss the methods used to probe this transition as well as briefly describing some of our findings in this system.

A. Methods

Our TCF apparatus with $\eta = 0.905$ was composed of a glass outer cylinder with a radius of $r_o = 80.03 \pm 0.02$ mm and a brass inner cylinder of radius $r_i = 72.39 \pm 0.01$ mm with a black powder coat to enhance optical contrast in flow visualization studies. The aspect ratio, $\Gamma = 5.26$, was set by two end caps, separated axially

by $h = 40.2 \pm 0.05$ mm and attached to rotate with the outer cylinder. The cylinders were driven by stepper motors; to reduce vibration and to ensure uniform cylinder rotation, timing belts connected the cylinders to the motors, which were mounted separately from the TCF apparatus. Additionally, a transmission with a gear ratio of 28:1 was used with the inner cylinder stepper motor to increase the resolution in Re_i. While the cylinders were rotating, the rate of temperature variations in the flow was kept below 0.5 °C throughout the duration of the experiments by surrounding the outer cylinder with a liquid bath. With these measures, the total systematic uncertainty for Re_i and Re_o was below 1 %.

In the tomo PIV results discussed here, determination of 3-D velocity fields were made throughout a flow volume with an approximate size of d radially, $0.75h$ axially, and $2\pi r_o/10$ azimuthally. Custom-made, density-matched polyester particles (25 µm to 32 µm in diameter) were doped with Rhodamine 6G and suspended in the flow. The particles were illuminated with a Quantronix 527/DP-H Q-switched Nd:YLF laser. Fluorescent light emitted from the particles was collected by four Vision Research Phantom V210 high speed cameras synchronized with the laser illumination. Each camera was fitted with a 105 mm Nikon Nikkor fixed focal length lens attached via a Scheimpflug adapter (LaVision Inc.). A low pass optical filter (Semrock BLP01-532R-25) on each camera lens attenuated, by a factor of 10^7, the scattered 527 nm wavelength laser illumination and passed, with 80% efficiency, fluorescent light at wavelengths >532 nm. The images were then analyzed using LaVision Inc.'s DaVis tomographic PIV software package. To reduce optical distortion from the outer cylinder's curved surfaces, the index of refraction of both the working fluid and the bath liquid were matched to the index of refraction of the glass outer cylinder. Index matching of the working fluid was achieved by using an ammonium thiocyanate solution prepared with a specific gravity of 1.13 and a kinematic viscosity of $\nu = 1.37$ mm^2/s at 23 °C [41]. A small amount of ascorbic acid was added to the ammonium thiocyanate solution to mitigate reaction with trace metals [42]. Index matching of the bath liquid was achieved by a binary mixture of two mineral oils with a 68.8 % heavy viscosity oil (McMaster-Carr part no. 3190K632) to 31.2 % light viscosity oil (McMaster-Carr part no. 3190K629) ratio. Further details about the implementation of tomo PIV measurements in our TCF apparatus are reported elsewhere [43].

Fully resolved direct numerical simulations (DNS) of TCF were conducted using the code developed by M. Avila and his collaborators [44–46]. This code uses a pseudospectral scheme to solve the Navier-Stokes equation in cylindrical coordinates subject to physical (no-slip) boundary conditions at the surface of the rotating concentric cylinders and top and bottom end caps. Details of how this code works can be found in Crowley *et al.* [17].

To quantify flow fields in both simulations and experiments, the perturbation flow field

$$\widetilde{\mathbf{v}}(t) = \mathbf{v}(t) - \mathbf{v}^{\mathrm{lam}}, \tag{5}$$

characterizes the deviation of the full flow $\mathbf{v}(t)$ from an axially symmetric laminar flow $\mathbf{v}^{\mathrm{lam}}$ computed numerically at the same Reynolds numbers. The numerically computed $\mathbf{v}^{\mathrm{lam}}$ was used to compute the perturbation flow field for both simulations and experiments since the laminar flow is unstable for some Re_i considered in this study, and, therefore, unobservable in the laboratory experiments.

B. Transition in experiments and numerics

First, we briefly describe a coarse experimental exploration of laminar-turbulent (turbulent-laminar) transitions that occur as Re_i is slowly increased (decreased) while maintaining Re_o fixed in the counter-rotating regime. We then focus on the case of $Re_o = -1000$ and examine in detail the transitions associated with increasing and decreasing Re_i using both laboratory experiments and numerical simulations.

1. Laminar-Turbulent Transition: Dependence on Re_o

To coarsely map out the transition boundaries for TCF in the geometry studied here, we performed flow visualization experiments by first spinning up the outer cylinder from rest (with the inner cylinder stationary) to a specific value of Re_o; then, with Re_o held constant, Re_i was increased in steps of $\Delta Re_i = 10$ by slowly stepping up the rotation rate of the inner cylinder until a qualitative change in the flow was observed. We

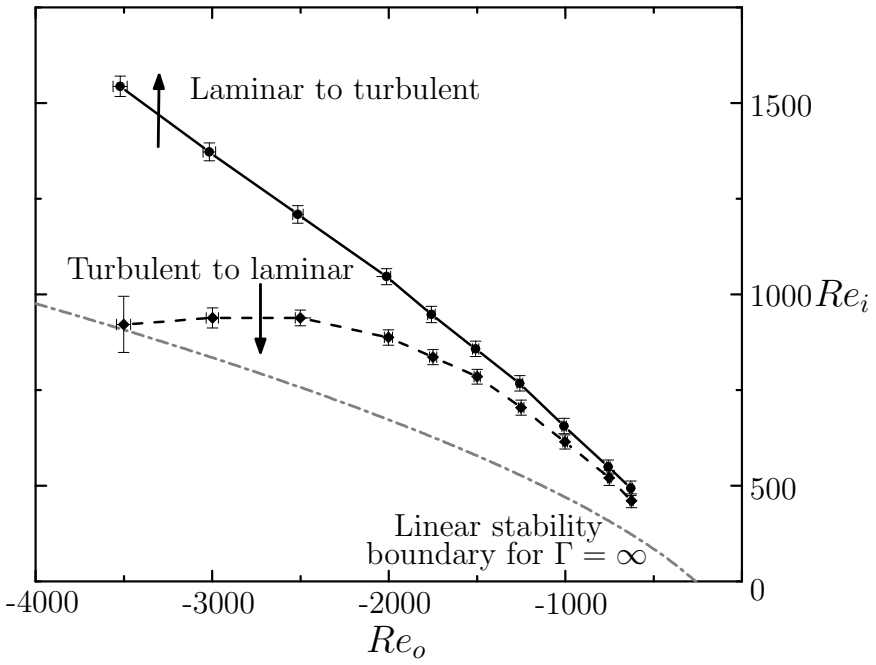

FIG. 6. Phase diagram illustrating the hysteretic laminar-turbulent transition in experiments on counter-rotating ($Re_o < 0$ and $Re_i > 0$) Taylor-Couette flow with $\Gamma = 5.26$ and $\eta = 0.905$. The diagram indicates transitions observed in experiments where Re_i was increased or decreased quasi-statically while keeping Re_o fixed. The black solid and dashed lines, drawn to guide the eye, indicate the transition boundaries from laminar flow to turbulence and from turbulence to laminar flow, respectively. The gray dash-dotted line represents the marginal stability curve for TCF at $\eta = 0.9$ for $\Gamma = \infty$ [47].

waited a time interval of $3.2\,\tau$ between steps to ensure that the flow had reached equilibrium. The turbulent-laminar transition boundary at the same Re_o was then determined by starting in the turbulent regime and slowing the inner cylinder down by $\Delta Re_i = 10$ every $3.2\,\tau$ until the flow was observed to be in the laminar state. The experiments were repeated for different fixed values of Re_o.

The experimental studies revealed instability of the azimuthally symmetric smooth laminar flow always leads to turbulence over a range of Re_o from -3500 to -500 (Figure 6). The transition back to laminar flow was always observed to be hysteretic; the range in Re_i over which hysteresis occurs increases as the magnitude of Re_o increases. Our results indicate that transition from laminar flow is suppressed by the moderate aspect ratio of our apparatus, i.e., for fixed Re_o, the transition occurs at Re_i larger than that predicted by linear stability analysis with $\Gamma = \infty$ (gray line in Figure 6). This observation is consistent with earlier experiments at larger values of Γ (and somewhat smaller values of η) where, like our studies, the end caps rotated with the outer cylinder [31]. In that work, the delay of laminar flow transition was found to increase with decreasing Γ, most likely due to the end-wall effects (e.g. dissipation and Ekman pumping) that become more pronounced as Γ decreases.

2. *Flow Transitions at $Re_o = -1000$*

A detailed experimental and numerical investigation at fixed $Re_o = -1000$ led to the observation of an intermediate state that plays an important role in the laminar-turbulent transition. The transition from turbulence to laminar flow was found to involve an aperiodic stable intermediate state (interpenetrating spirals) that persists over a range of Re_i. Moreover, IPS were found to appear – albeit transiently – during the transition from laminar flow to turbulence. Transitions between different flow states are described in detail below.

a. Transitions in Laboratory Experiments

Transition	Experiment	Noiseless DNS
Laminar → Turbulence	643 ± 2	675 ± 5
Turbulence → IPS	625 ± 3.6	623.5 ± 0.5
IPS → Turbulence	631 ± 3.7	630.5 ± 0.5
IPS → Laminar	617 ± 1	617.5 ± 0.5

TABLE I. The inner cylinder Reynolds numbers for flow transitions are shown for both laboratory experiments and numerical simulations at $Re_o = -1000$. Uncertainty values from the experiment reflect the systematic uncertainties associated with the measurement of Re as well as repeatability of the transition, while the uncertainty values from the noiseless DNS reflect the resolution with which the dependence on Re_i was investigated. The uncertainties in experimental values were calculated using an uncorrelated linear propagation of uncertainties associated with all measured quantities and measurement repeatability represented by the standard deviation.

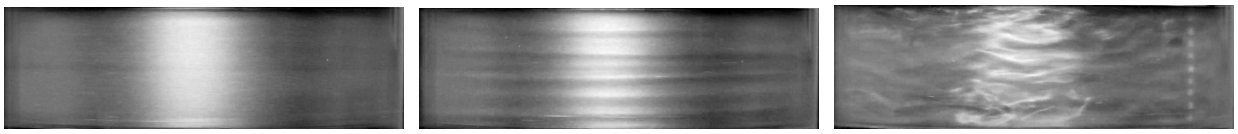

(a) (b) (c)

FIG. 7. Evolution of the flow during laminar to turbulent transition in experiments at $Re_o = -1000$ and $Re_i = 643$. The sequence of snapshots shows (a) the initial laminar flow, (b) transient interpenetrating spirals, and (c) persistent intermittent turbulence.

Transitions were determined in flow visualization studies by first spinning up the outer cylinder to $Re_o = -1000$ (with the inner cylinder at rest), and then increasing the inner cylinder's counter-rotation in steps of $\Delta Re_i = 0.5$ every $3.2\,\tau$, until the flow became turbulent. Subsequently, beginning from the turbulent state, Re_i was decreased at the same rate as before until the flow returned to the laminar state. No observable shifts in the transition boundaries were found when incrementing or decrementing Re_i in steps of $\Delta Re_i = 0.25$ separated in time by $10.7\,\tau$.

With the flow starting in a laminar state, laboratory experiments exhibit a laminar-turbulent transition at $Re_i = 643$ with a total uncertainty in Re_i of ± 2. Repeated measurements demonstrate the transition can be observed with a resolution of ± 0.13 (i.e. 0.02 %), as constrained by the mechanical limits of the motor and transmission driving the inner cylinder; in other words, from laminar flow just below threshold (cf. Figure 7(a)), a single increment of $\Delta Re_i = 0.13$ results in turbulence. At onset (with Re_i fixed), the structure of the flow changes slowly at first; very weak interpenetrating spirals gradually become discernible and grow slowly in amplitude with time (cf. Figure 7(b)). Then, abruptly, the spirals break up and spatiotemporally intermittent turbulence develops on top of an IPS-like background flow and persists (cf. Figure 7(c)). The interval of time over which the flow resembles IPS before transitioning to turbulence was different each time the experiment was performed and this interval decreased with an increase in the increment size of ΔRe_i. If Re_i is increased stepwise (with a fixed time interval of $3.2\,\tau$ between each step), the transition Re_i is unchanged for increments of $\Delta Re_i < 1$; the transition Re_i is observed to decrease for increments of $\Delta Re_i > 1$.

Starting from turbulent flow, decreasing Re_i reveals a transition to stable IPS at $Re_i = 625 \pm 3.6$. IPS were observed to be weakly chaotic (i.e., having a broad-band temporal spectrum) over a range of Re_i and persist for as long as $3.8 \times 10^3\,\tau$ (two and a half days, after which time the experiments were ended). From stable IPS, increasing Re_i leads to a transition back to intermittent turbulence at $Re_i = 631 \pm 3.7$; decreasing Re_i leads instead to a transition to the axisymmetric laminar state at $Re_i = 617 \pm 1$. It should be noted that the values of Re_i at which various transitions are observed (see Table I) depend on disturbances of two qualitatively different types: (a) disturbances associated with a discrete change of Re_i and (b) other types of disturbances (e.g., the cylinders not being perfectly round or coaxial, the deviation in their angular velocity from a constant, etc.). All of these are disturbances of a finite, though likely small, amplitude.

b. Transitions in Numerical Simulations

Numerical simulations were used to determine linear stability of the steady axisymmetric laminar flow $\mathbf{v}^{\mathrm{lam}}$. This flow was generated at $Re_o = -1000$ and different fixed Re_i by keeping only the azimuthally symmetric mode and evolving the state until it stopped changing. The azimuthal symmetry of this flow was then broken

by perturbing the first Fourier mode (with the nonlinear term generating disturbances for all other modes). Evolving the perturbed flow, we found that the perturbation decays (the laminar state is linearly stable) for $Re_i < Re_i^c = 675 \pm 5$ and grows, resulting in a transition to turbulence, for $Re_i > Re_i^c$.

Since the laminar flow undergoes transition to turbulence in experiment at a notably lower Re_i than the linear stability threshold Re_ic, an investigation of its stability to finite amplitude disturbances was performed. Qualitatively, we find that, for $Re_i \geq 634$, finite amplitude perturbations lead to destabilization of the laminar state, giving rise to IPS with an amplitude that grows and saturates temporarily. Ultimately the IPS gives way to spatiotemporally intermittent turbulence, just as in the experiment. Qualitatively the same transition sequence was found to occur for initial disturbances with different magnitudes and spatial profiles.

To quantify qualitatively how the critical disturbance amplitude depends on Re_i, we fixed the spatial profile of the disturbance by choosing the initial condition in the form of a homotopy

$$\mathbf{v} = (1-\alpha)\mathbf{v}^{\mathrm{lam}} + \alpha \mathbf{v}^{\mathrm{IPS}}, \tag{6}$$

where $\mathbf{v}^{\mathrm{lam}}$ is the laminar flow at the given Re_i and $\mathbf{v}^{\mathrm{IPS}}$ is a snapshot of the (nonaxisymmetric) IPS at $Re_i = 630$. The structure of the IPS is fairly similar at different Re_i; thus, for the purpose of determining critical disturbance amplitudes, we considered it to be sufficient to compute $\mathbf{v}^{\mathrm{IPS}}$ at a fixed Re_i. The homotopy parameter $0 \leq \alpha \leq 1$ characterizes the magnitude of the disturbance; increasing α increases the disturbance amplitude. This particular choice of homotopy guarantees that initial conditions are divergence-free for any value of α.

Numerical simulations find the same sequence of transitions as laboratory experiments when the flow is initially turbulent. Decreasing Re_i first leads to a transition to stable IPS at $Re_i = 623.5 \pm 0.5$. From stable IPS, increasing Re_i leads to a transition back to turbulence at $Re_i = 630.5 \pm 0.5$, while decreasing Re_i leads to a transition to the time-independent laminar state at $Re_i = 617.5 \pm 0.5$. These numerically determined transition Reynolds numbers between IPS and turbulence and from IPS to laminar are quantitatively in agreement with those found in laboratory experiments, as illustrated in Table I. Due to the subcritical nature of the transition between laminar and turbulence, however, the appropriate choice of the finite amplitude perturbation, α, is required.

The protocol for determining Re_i for transition from turbulence to IPS is as follows: We started with verifying that turbulence persists at $Re_i = 640$ by evolving the flow for a time interval $5.264\,\tau$. Then we ramped down Re_i in increments of $\Delta Re_i = 5$ and evolved the flow for the same interval to determine whether a transition occurred. Once a transition was detected (at $Re_i = 620$), we re-initialized the flow using the final state of the simulation at $Re_i = 625$, decreased the Reynolds number by $\Delta Re_i = 1$, and evolved the flow for a further $5.264\,\tau$. The procedure was repeated with $\Delta Re_i = 2, 3, \cdots$ until a transition was found.

A similar protocol was used for the two transitions from stable IPS. In these cases, we verified that stable IPS persists at $Re_i = 620$ and 630. The final states of the simulation at $Re_i = 630$ (or $Re_i = 620$) were evolved for $5.264\,\tau$ at a fixed Re_i that was increased (or decreased) by $\Delta Re_i = 1, 2, 3, \cdots$ until transition to turbulence (or laminar flow) was found. Note that, in all of these cases, only one simulation was performed and the finest resolution was $\Delta Re_i = 1$, which determines the accuracy of the values reported in Table I.

Given ample experimental evidence that the transitions between turbulence and IPS are probabilistic [17], we did not investigate these transitions numerically in more detail. For the transition from IPS to laminar flow, however, experiments did not conclusively determine the nature of the transition. We therefore performed an additional numerical investigation of this transition by evolving IPS at a number of fixed Re_i in the range $(617, 618)$. While most of the results were consistent with a transition threshold found previously, there were a few outliers. In particular, we found that evolving IPS for $5.264\,\tau$ at $Re_i = 617.8125$ does not result in a transition to a laminar flow, although eventually the flow does relaminarize. This result shows that the transition from IPS to laminar flow also appears to have a probabilistic nature and does not correspond to a bifurcation which would have resulted in a sharp transition boundary.

c. Flow Field Characterization

Flow fields computed numerically also compare well with measurements from laboratory experiments. The stable IPS found in simulations and experiments exhibit a similar spatial structure (Figure 8). Moreover, both experiments and simulations show that just above the onset of turbulence, the flow features localized patches of turbulence that co-exist with disordered spiral structures [17] (see Figure 8 for an example of the localized turbulent patch in both experiment and numerics). To quantitatively compare the flows in

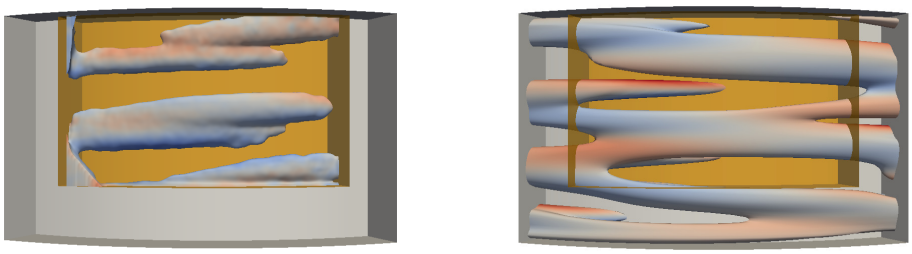

(a) (b)

FIG. 8. A snapshot of interpenetrating spirals in (a) a tomo PIV experiment and (b) DNS. Each image shows a single isosurface of the perturbation field, $\widetilde{\mathbf{v}}_\theta$, for $Re_i = 625$ and $Re_o = -1000$ inside a cylindrical subvolume. The color indicates the corresponding azimuthal velocity component. Red (blue) indicates flow in the same direction as the inner (outer) cylinder rotation. The shaded orange rectangular box represents the region probed by tomo PIV, which spans approximately 10 % of the flow domain volume.

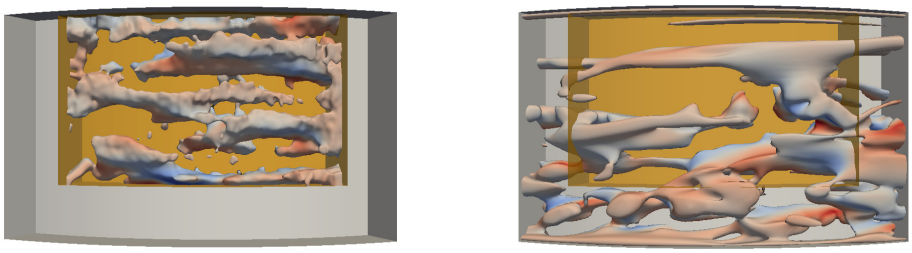

(a) (b)

FIG. 9. A snapshot of a turbulent flow in experiment (a) and DNS (b). Each image shows a single isosurface of the perturbation field, $\widetilde{\mathbf{v}}_\theta$, for $Re_i = 650$ and $Re_o = -1000$ inside a cylindrical subvolume. The color indicates the corresponding azimuthal velocity component. Red (blue) indicates flow in the same direction as the inner (outer) cylinder rotation. The shaded orange rectangular box represents the region probed by tomo PIV, which spans approximately 10 % of the flow domain volume.

experiment and numerics, we computed the average energy E corresponding to the θ component of the velocity perturbation $\widetilde{\mathbf{v}} = \mathbf{v} - \mathbf{v}^{\text{lam}}$ over a time interval $T = O(\tau)$ and region Ω in the r, z plane at a fixed azimuthal location where experimental velocity measurements were available. Only the θ-component of velocity was analyzed because v_r and v_z had increased noise due to the frame rates used in the PIV. The region Ω is bounded by the coordinates $r \in [\eta/(1-\eta), 1/(1-\eta)]$ and $z/\Gamma \in [0.254, 0.973]$, where z is measured from the bottom of the flow domain. For the stable states (IPS and turbulence), the average energy was defined according to

$$E = \frac{1}{TA} \int_0^T dt \int_\Omega \widetilde{v}_\theta^2(t)\, dr dz, \tag{7}$$

where A is the area of the cross section of Ω.

The information presented above is summarized in Fig. 10 in the form of a bifurcation diagram. In particular, we find that the energy E serves as a good order parameter that allows one to easily distinguish the qualitatively different flows (laminar flow, IPS, and turbulence) and to determine where transitions between different flows take place. In particular, we find that the average values of E in experiment and numerics are in good quantitative agreement and that E changes smoothly with Re_i for both IPS and turbulent flow over the regions where these flows are stable (indicated by solid black lines). The dashed lines indicate the trends when these flow states become unstable and are merely extrapolations of the solid curves.

The figure also shows how the energy of the critical disturbance that lies on the boundary of the basin of

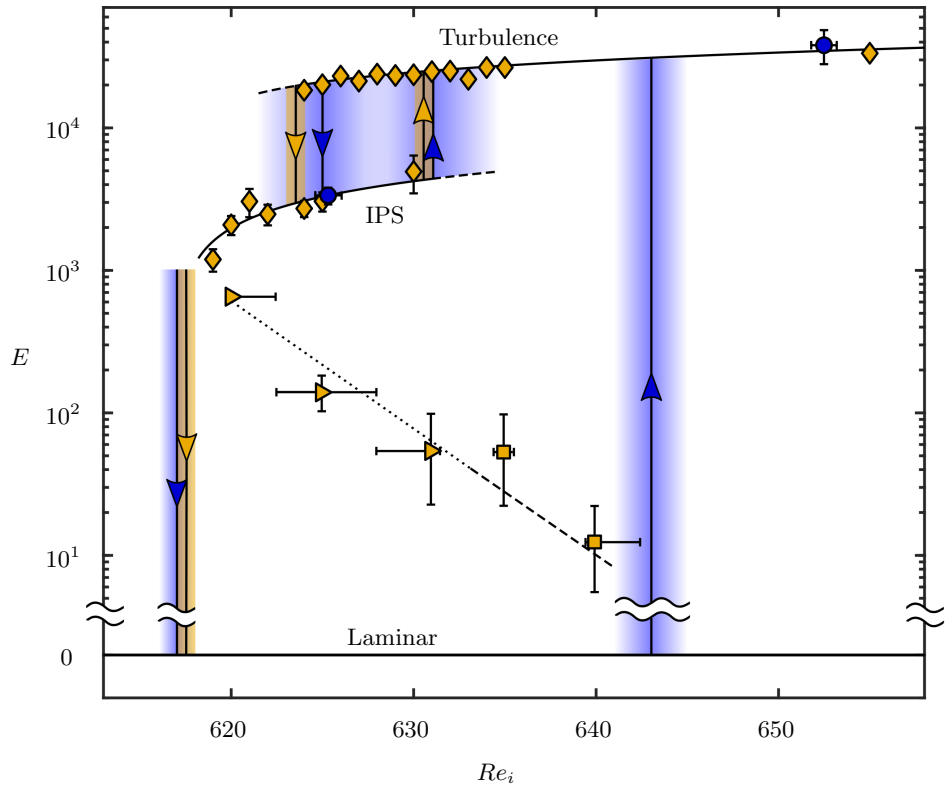

FIG. 10. Transition map for the three flow states: laminar, IPS, and turbulence. Numerically computed values of E for stable IPS and turbulence at various Re_i are plotted as ♦ while the values calculated from experimental measurements are plotted as ●. The gold and blue arrows indicate the values of Re_i at which transitions occur in simulation and experiment respectively. The shading around the arrows corresponds to the uncertainty in the transitional Re_i value. The ▷ and ▫ represent the E value associated with the critical magnitude of the finite amplitude perturbation considered here, which corresponds to $\alpha = \alpha_c$, necessary to initiate transition from laminar flow to IPS and turbulence, respectively. All curves are to guide the eye only.

attraction of the stable laminar flow varies with Re_i. The dotted (dashed) line denotes the transition to IPS (turbulence). To compute this boundary, we performed an average over the azimuthal variable rather than time in (7), where $\widetilde{\mathbf{v}} = \alpha(\mathbf{v}^{\mathrm{IPS}} - \mathbf{v}^{\mathrm{lam}})$ according to (6) and $\alpha = \alpha_c$. Although the specific values of E which define this boundary, just like α_c, depend on the spatial structure of the perturbation $\widetilde{\mathbf{v}}$, the shape of the boundary suggests that it is related to an unstable edge state (or states) connecting the laminar state and IPS, as discussed previously.

In the course of this work we learned that the transition to turbulence in a TCF with $\Gamma = 5.26$ is direct from laminar to turbulent, unlike the transition observed in large aspect ratio systems. This transition is mediated by an intermediate flow state that believed to live on the boundary between turbulence and laminar. The direct nature of this transition resembles the transitions to turbulence observed in wall bounded, shear flows which makes the small Γ TCF an interesting system to study the dynamical systems description of turbulence.

IV. PROPOSED WORK: EXPERIMENTAL SEARCH FOR ECS IN TURBULENT TCF

The aim of this research is to show that a real turbulent flow can be understood in the dynamical systems framework that is discussed in section II A. Other studies have investigated this dynamical systems framework, however it has been done by and large in numerics [12–16]. Experimental observations of close passes to ECS, on the other hand, have mostly been either in 2D flows [48, 49] or in 3D flows with ambiguous

comparison techniques [50, 51]. The ambiguities present in previous studies can be removed by working in TCF in a limit where the numerics are able to compute the entire flow field, incorporating the physical boundary conditions and the experiment can make time-resolved measurements of the velocity field in a sufficiently large region of the laboratory flow.

In order to test the dynamical systems description of turbulence experimentally, a process needs to be specified for identifying the key solutions that influence the flow in state space, namely the ECSs. The challenge with identifying the ECS is that they are not known *a priori* and need to be first discovered then characterized. Once the ECSs are identified, a means of observing a turbulent trajectory making a close pass to an ECS in state space is needed. This ability to identify when the turbulent flow is dynamically close to an ECS could be an essential tool needed to further develop a dynamical systems approach to understanding turbulence.

Candidate ECSs to be tested experimentally need to first be identified numerically. To do this, a long turbulent time series computed in numerics can be generated and analyzed for key features of an ECS. The snapshot in time where the numerical turbulent trajectory exhibits the key features of an ECS can then be used as an initial condition in an optimization algorithm to converge onto the ECS that is nearby in state space [52]. In general, there is no single identifying feature that could be easily looked for in a turbulent record, thus each class of ECS needs to be searched for with different tools. For instance, if the ECS was a fixed point (e.g. point C in figure 2), than a close pass in state space would mean that the time evolution of a trajectory would become more and more time-independent as it got closer. This means that a graph of the turbulent trajectories speed moving through state space can be searched for regions where the speed drop close to zero. Preliminary evidence, however, suggests that fixed points do not play a key role in the dynamics of state space for TCF, but instead, the dynamics are influenced by periodic orbits. Periodic orbits are solutions in state space that form closed loops. This means that as time evolves, the flow will repeat itself.

For periodic ECS, a tool called the self-recurrence can be used to find good initial conditions for a convergence algorithm. An ECS that is periodic in time would exhibit self similarity at a time separated by the period of the ECS. This key feature of a periodic orbit can be used as a signature to identify the proximity of a turbulent trajectory to this class of ECS. To exploit this signature, a metric of self similarity, or self-recurrence, can be defined as:

$$\mathcal{R}_{\text{self}}(t, t-t') = min_{\phi}||\vec{u}_{\text{turb}}(r,\theta,z,t) - R_{\phi}\vec{u}_{\text{turb}}(r,\theta,z,t-t')|| \tag{8}$$

where t' is the time delay, R_ϕ applies a shift by ϕ along the azimuthal direction to account for possible drifts of the flow structure, and $||\cdot||$ is the norm of the vector. This self-recurrence is a function of both time along the turbulent trajectory, t and an earlier time, $t-t'$. Once $\mathcal{R}_{\text{self}}(t, t-t')$ is computed, a heat-map where the intensity of each pixel corresponds to the value of $\mathcal{R}_{\text{self}}$ at that value of $(t, t-t')$ can be generated. An example of a this self-recurrence plot can be seen in figure 11. In these plots, nearly periodic intervals of the turbulent series show up as periodic structures in the horizontal and vertical direction. Regions of the turbulent trajectory where the self-recurrence plot shows particularly strong periodic structure can be used as an initial condition for an algorithm that searches in state space for time periodic flows. Some of the initial conditions obtained this way converge to an ECS.

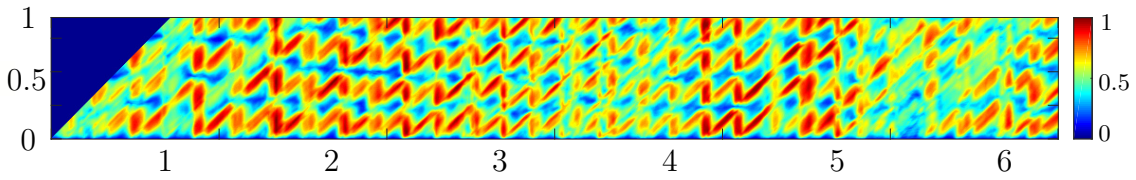

FIG. 11. Example self-recurrence plot of a simulated turbulent trajectory at $Re_o = -200$ and $Re_i =$ in TCF with $\Gamma = 1$ and $\eta = 0.71$. Figure adapted from Krygier [52]

A cross-recurrence shows whether or not the turbulent trajectory mimics the ECSs behavior. Once an ECS has been obtained, the next step is to observe that not only does the turbulent flow come near the

ECS in state space, but the turbulence also mimics its dynamics. This can be done by evaluating what is called the cross-recurrence between the turbulence and the ECS. The cross-recurrence is very similar to the self-recurrence, except that it is comparing the difference between the turbulence and a particular known ECS. Thus, the cross-recurrence is given by

$$\mathcal{R}_{\text{cross}}(t,\tau) = min_{\phi}||\vec{u}_{\text{turb}}(r,\theta,z,t) - R_{\phi}\vec{u}_{\text{ECS}}(r,\theta,z,\tau)|| \tag{9}$$

where τ is the phase along the periodic orbit. From $\mathcal{R}_{\text{cross}}$, similar plots to those made to initially identify periodic ECS are generated. If the turbulent trajectory is close and also mimicking the behavior of the ECS, than the flow and ECS will be evolving at the same rate. This means a close pass will have a minimum that is elongated along the diagonal (i.e. $t = \tau$). An example of a close pass seen in the cross-recurrence of numerically computed turbulence and an ECS can be seen in figure 12.

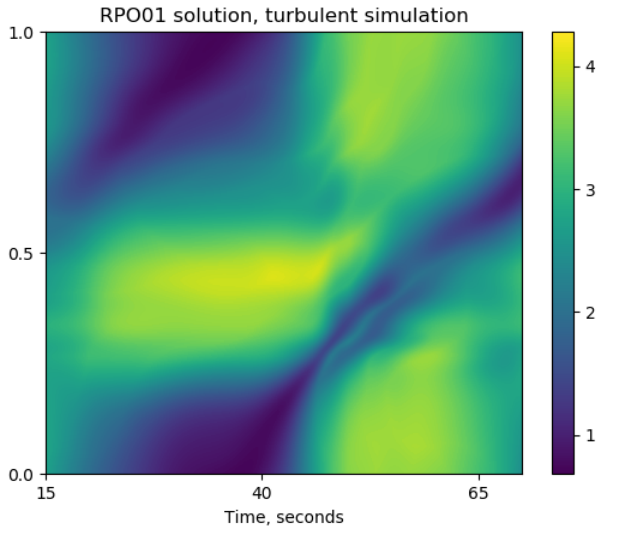

FIG. 12. Example of a cross-correlation between numerical integrated turbulence and an ECS. Note the minimum that occurs along a diagonal is characteristic of a close pass to a relative periodic orbit.

Currently, seven candidate ECSs to be compared with experimentally obtained turbulent flows have been identified. The process for evaluating the dynamical relevance of an ECS in the experimental flow is, in essence, the same as what was done in numerics. That is, a cross-recurence between the experimentally measured turbulence and and ECS will be evaluated and searched for minima that fall along the diagonal. There are, however, a few considerations that need to be discussed that are specific to how this will be done in experiment.

The first consideration is what the system will allow for measurements of turbulent flow that can be compared to the ECS. I propose designing and constructing a new, small aspect ratio TCF to perform this search for ECS. This new TCF would be constructed completely out of transparent, index matched materials allowing for optical access to 100 % of the flow domain. With optical access to the full flow domain, either full volumetric velocity measurements or 2D-2C measurements in selected planes of the flow can be performed. This system would allow for direct comparisons of the full numerically computed ECS with full flow field measured in experiment. To obtain full volume velocity measurements, cameras can be aimed from beneath the experiment and frame rates could be designed to be low enough to allow for the images to be streamed directly to disk allowing for extended observation times. Similarly, to obtain 2D-2C velocity measurements, a light sheet could shine through the side walls of the experiment and a camera placed directly bellow it could record the motion of particles in the light sheet. An example of this proposed design can be seen in Fig. 13.

Before making full domain measurements of turbulence, PIV obtained on a thin slice (2D-2C) at a constant z height will be compared to the ECS. The simplified nature of the 2D-2C measurements is advantageous for the development of the procedures as well as the computational machinery needed to make comparisons

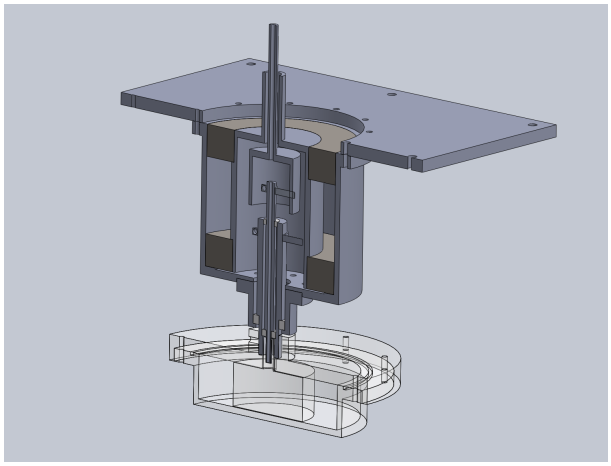

FIG. 13. Drawing of proposed new Taylor-Couette cell and mounding assembly. The cell at the bottom would be constructed out of acrylic to be both transparent and index matched to working and cooling fluids. The assembly in gray is the broken axle drive shafts.

to the numerics. By measuring the in-plane velocity of the r-θ plane, flow information along the entire symmetry dimension will be obtained. This will reduce ambiguities along the streamwise direction, but information along the z-axis will not be present. However, cross-recurrences with numerically integrated turbulence against known ECS performed with only the in-plane components along the r-θ plane in the center of the domain showed similar results to the full 3D cross-recurrence of the same data. Therefore, no extrapolation or approximation technique will be implemented.

Although no extrapolation is needed, choosing the proper plane in numerics that corresponds to the experiment is crucial. The PIV data will be obtained in a plane very near the center of the domain, but a change in the location along z of only 1 mm results in discrepancies too large to properly perform recurrence analysis. To overcome this, axisymmetric laminar flow in the experiment will be measured in conjunction with each experimental turbulence experiment and compared with the numerically computed laminar flow at the same Reynolds numbers. By minimizing the difference between the experimentally obtained velocity profile and the numerically computed profile, the z height can be determined to high accuracy.

[1] J. Lumley, Physics of Fluids A: Fluid Dynamics **4**, 203 (1992).
[2] G. G. Stokes, On the effect of the internal friction of fluids on the motion of pendulums, in *Mathematical and Physical Papers*, Cambridge Library Collection - Mathematics, Vol. 3 (Cambridge University Press, 2009) p. 1–10.
[3] F. R. Hama, J. D. Long, and J. C. Hegarty, Journal of Applied Physics **28**, 388 (1957).
[4] A. F. Hussain, The Physics of fluids **26**, 2816 (1983).
[5] W. Willmarth and B. J. Tu, The Physics of Fluids **10**, S134 (1967).
[6] S. K. Robinson, Annual Review of Fluid Mechanics **23**, 601 (1991).
[7] B. A. Singer and R. D. Joslin, Physics of Fluids **6**, 3724 (1994).
[8] D. Rockwell and E. Naudascher, Annual Review of Fluid Mechanics **11**, 67 (1979).
[9] P. Cvitanović, R. Artuso, R. Mainieri, G. Tanner, and G. Vattay, *Chaos: Classical and Quantum* (Niels Bohr Institute, Copenhagen, 2016).
[10] J. Jiménez, Journal of Fluid Mechanics **842**, P1 (2018).
[11] F. Waleffe, Physics of Fluids **9**, 883 (1997).
[12] F. Waleffe, in *Turbulence and Interactions*, edited by M. Deville, T.-H. Lê, and P. Sagaut (Springer Berlin Heidelberg, Berlin, Heidelberg, 2009) pp. 139–158.
[13] H. Faisst and B. Eckhardt, Phys. Rev. Lett. **91**, 224502 (2003).
[14] M. Avila, F. Mellibovsky, N. Roland, and B. Hof, Phyical Review Letters **110**, 224502 (2013).
[15] K. Deguchi, A. Meseguer, and F. Mellibovsky, Phys. Rev. Lett. **112**, 184502 (2014).
[16] J. F. GIBSON, J. HALCROW, and P. CVITANOVIĆ, Journal of Fluid Mechanics **638**, 243–266 (2009).
[17] C. J. Crowley, M. C. Krygier, D. Borrero-Echeverry, R. O. Grigoriev, and M. F. Schatz, Journal of Fluid Mechanics **892**, A12 (2020).
[18] H. Poincaré, *New Methods of Celestial Mechanics*, 1st ed., 13 (AIP-Press, Melville, NY, 1992).
[19] in *Chaos: Classical and Quantum*, edited by P. Cvitanović, R. Artuso, R. Mainieri, G. Tanner, and G. Vattay (Niels Bohr Institute, 2012) 16th ed., Chap. A1.
[20] N. Bacaër, in *A short history of mathematical population dynamics* (Springer, 2011) pp. 71–76.
[21] B. Suri, L. Kageorge, R. O. Grigoriev, and M. F. Schatz, Phys. Rev. Lett. **125**, 064501 (2020).
[22] L. Rayleigh, Proceedings of the Royal Society of London. Series A, Containing Papers of a Mathematical and Physical Character **93**, 148 (1917).
[23] S. Chandrasekhar, *Hydrodynamic and hydromagnetic stability* (Courier Corporation, 2013).
[24] G. I. Taylor, Philosophical Transactions of the Royal Society of London. Series A, Containing Papers of a Mathematical or Physical Character **223**, 289 (1923).
[25] F. Schultz-Grunow and H. Hein, Z. Flugwiss **4**, 28 (1956).
[26] C. D. Andereck, S. S. Liu, and H. L. Swinney, Journal of Fluid Mechanics **164**, 155 (1986).
[27] D. Borrero-Echeverry, C. J. Crowley, and T. P. Riddick, Physics of Fluids **30**, 087103 (2018).
[28] D. Coles, Journal of Fluid Mechanics **21**, 385 (1965).
[29] A. Prigent and O. Dauchot, in *IUTAM Symposium on Laminar-Turbulent Transition and Finite Amplitude Solutions*, edited by T. Mullin and R. Kerswell (Springer Netherlands, Dordrecht, 2005) p. 195.
[30] D. Borrero-Echeverry, M. F. Schatz, and R. Tagg, Physical Review E **81**, 025301(R) (2010).
[31] C. F. Hamill, *Turbulent bursting in the Couette-Taylor system*, Master's thesis, University of Texas at Austin (1995).
[32] M. Raffel, C. E. Willert, F. Scarano, C. J. Kähler, S. T. Wereley, and J. Kompenhans, *Particle image velocimetry: a practical guide* (Springer, 2018).
[33] L. Adrian, R. J. Adrian, and J. Westerweel, *Particle image velocimetry*, 30 (Cambridge university press, 2011).
[34] J. Estevadeordal, C. Marks, R. Sondergaard, and M. Wolff, Experiments in fluids **50**, 761 (2011).
[35] G. T. Herman and A. Lent, Computers in Biology and Medicine **6**, 273 (1976), advances in Picture Reconstruction;Theory and Applications.
[36] B. Wieneke, Measurement Science and Technology **24**, 024008 (2012).
[37] G. E. Elsinga, F. Scarano, B. Wieneke, and B. W. van Oudheusden, Experiments in Fluids **41**, 933 (2006).
[38] G. E. Elsinga, B. Wieneke, F. Scarano, and A. Schröder, Tomographic 3d-piv and applications, in *Particle Image Velocimetry: New Developments and Recent Applications* (Springer Berlin Heidelberg, Berlin, Heidelberg, 2008) pp. 103–125.
[39] S. Discetti and T. Astarita, Experiments in fluids **53**, 1437 (2012).
[40] M. Novara, A. Ianiro, and F. Scarano, Measurement Science and Technology **24**, 024012 (2012).
[41] D. Borrero-Echeverry and B. C. A. Morrison, Experiments in Fluids **57**, 123 (2016).
[42] J. Sommeria, S. D. Meyers, and H. L. Swinney, in *Nonlinear Topics in Ocean Physics*, Enrico Fermi International School of Physics, Vol. 109, edited by A. Osborne (North-Holland, Amsterdam, 1991) p. 227.
[43] D. Borrero-Echeverry, *Subcritical transition to turbulence in Taylor-Couette flow*, Ph.D. thesis, Georgia Institute of Technology (2014).

[44] M. Avila, M. Grimes, J. M. Lopez, and F. Marques, Physics of Fluids **20**, 104104 (2008).
[45] I. Mercader, O. Batiste, and A. Alonso, Computers & Fluids **39**, 215 (2010).
[46] M. Avila, Physical Review Letters **108**, 124501 (2012).
[47] A. Esser and S. Grossmann, Physics of Fluids **8**, 1814 (1996).
[48] B. Suri, J. Tithof, R. O. Grigoriev, and M. F. Schatz, Physical Review Letters **118**, 114501 (2017).
[49] B. Suri, R. K. Pallantla, M. F. Schatz, and R. O. Grigoriev, Phys. Rev. E **100**, 013112 (2019).
[50] B. Hof, C. W. H. van Doorne, J. Westerweel, F. T. M. Nieuwstadt, H. Faisst, B. Eckhardt, H. Wedin, R. R. Kerswell, and F. Waleffe, Science **305**, 1594 (2004).
[51] G. Lemoult, K. Gumowski, J.-L. Aider, and J. E. Wesfreid, The European Physical Journal E **37**, 25 (2014).
[52] M. C. Krygier, *Exact coherent structures in turbulent small-aspect-ratio Taylor-Couette flow*, Ph.D. thesis, Georgia Institute of Technology (2019).